Multi-degree-of-freedom spherical permanent-magnet gravity compensator for mobile arm support systems

Multi-Degree-of-Freedom Spherical Permanent-Magnet Gravity Compensator for Mobile Arm Support Systems

B. van Ninhuijs, *Student Member, IEEE*, J. W. Jansen, *Member, IEEE*, B. L. J. Gysen, *Member, IEEE*, and E. A. Lomonova, *Senior Member, IEEE*

***Abstract*—This paper presents a magnetic gravity compensator, which is able to provide compensation about two axes of rotation for mobile arm support systems. Because of the compensation about two axes, it provides more flexibility than the existing mechanical gravity compensators. This flexibility is achieved by using two semispherical permanent magnets, where the inner semisphere can rotate about the x-, y-, and z-axis with respect to the outer semisphere. Several magnetization topologies, which are evaluated using 2-D finite-element analysis (FEA), are investigated, and the most suitable topology is optimized in 2-D FEA. The optimization results are verified with 3-D FEA.**

***Index Terms*—Finite-element analysis (FEA), gravity compensation, permanent magnets, semisphere.**

I. Introduction

MOBILE arm support systems provide aid during activities of daily living (ADL), such as eating, drinking, and using a computer, for people with limited muscle activity. The limited muscle activity can be caused by, e.g., a neuromuscular disease or a stroke, and results in difficulties to overcome the gravity. Therefore, mobile arm support systems use gravity compensation to enhance human capabilities to perform ADL more independently. These support systems are used at home and can be mounted on a table, chair, or electric wheelchair. In each of these cases, no or limited electrical energy is available; therefore, passive (consumption of energy is zero) gravity compensation is beneficial. The currently available passive gravity compensators use mechanical springs, which are prestressed [1], [2]. These springs provide adjustable gravity compensation about a single axis. The compensation is adjusted using an electrical actuator, which varies the spring tension.

Using electrical actuators to provide support during ADL results in bulky and cumbersome arm support systems [3], [4], which is disadvantageous for use at home. The arm support becomes bulky because several single degree-of-freedom actuators are used for the shoulder joint alone. Utilizing multiple degree-of-freedom actuators can decrease the mass and voluminousness of the arm support, where spherical actuators could be used because they can mimic the shoulder joint. Existing spherical actuator concepts with a rotor radius between 31 and 60 mm produce a torque of about 4 N · m [5]–[9], which is insufficient for arm support systems. Higher torque can be achieved by increasing the complexity, for example, a rotor radius of 137 mm, 96 separately excited coils, 112 permanent magnets, and a torque production of 40 N · m [10]. This torque level is sufficient for arm support systems; however, due to the large amount of separately excited coils, and thus required power electronics, it is not suitable for mobile arm applications.

To achieve the desired torque density and multiple degrees of freedom, a novel passive spherical permanent-magnet gravity compensator is proposed. Linear magnetic gravity compensators are already investigated for applications, such as automotive [11] and high-precision applications [12], [13]. The proposed spherical permanent-magnet gravity compensator consists of two semispherical permanent magnets, as shown in Fig. 1. These spherical shapes provide compensation about two axes, which increases the flexibility compared with existing mechanical compensators. Subscript s in this figure denotes the stationary coordinate system of the spherical gravity compensator.

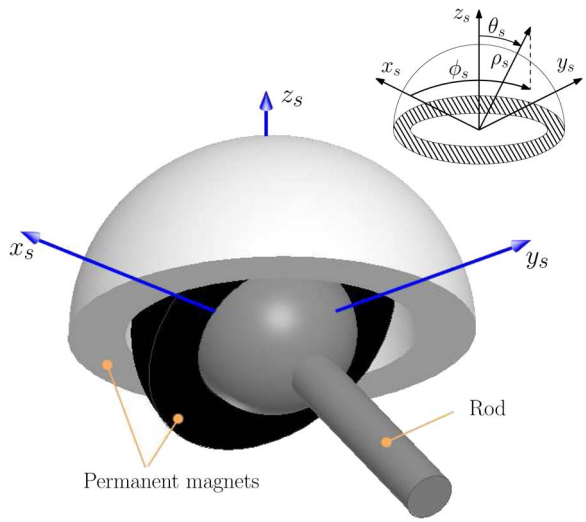

Fig. 1. Proposed spherical permanent-magnet gravity compensator.

Manuscript received August 2, 2013; revised December 18, 2013; accepted February 11, 2014. Date of publication March 21, 2014; date of current version November 18, 2014. Paper 2013-EMC-569.R1, presented at the 2013 IEEE International Electric Machines and Drives Conference, Chicago, IL, USA, May 12–15, and approved for publication in the IEEE Transactions on Industry Applications by the Electric Machines Committee of the IEEE Industry Applications Society. This work was supported by the Dutch "Pieken in de Delta" Program, under Project McArm PID102055, which is financed by Agentschap NL and Provinces Noord Brabant and Limburg.

The authors are with the Department of Electrical Engineering, Group of Electromechanics and Power Electronics, Eindhoven University of Technology, 5612 AZ Eindhoven, The Netherlands (e-mail: b.v.ninhuijs@tue.nl).

Color versions of one or more of the figures in this paper are available online at http://ieeexplore.ieee.org.

Digital Object Identifier 10.1109/TIA.2014.2313066

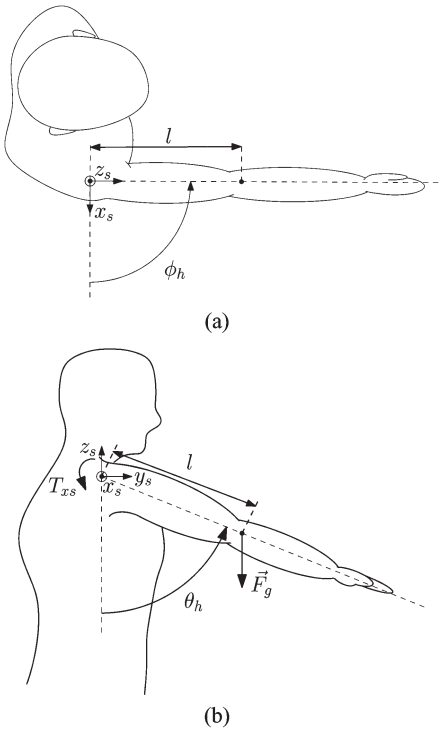

Fig. 2. Schematic representation of a human upper limb and the torque generated by the shoulder joint. (a) Top view. (b) Side view.

TABLE I
SPECIFICATIONS

Parameter	Value	Unit	Description
m	3	kg	arm mass
l	0.4	m	lever-arm distance
T_{max}	12	Nm	maximum torque
θ_h	0-90	degree	flexion/abduction movement
ϕ_h	40-130	degree	horizonal abduction movement

The necessary torque characteristics are analyzed for gravity compensation in arm support systems. Different magnetization topologies are investigated using 2-D finite-element analysis (FEA) to satisfy the required torque properties. It is shown that 2-D finite element can be used to represent the 3-D model. From this 2-D FEA, the most suitable topology is optimized for the arm support application. The obtained results of the optimized topology is verified using 3-D FEA. Finally, from these results, a conclusion is given for the application of the proposed topology in arm support systems.

II. SPECIFICATIONS

The shoulder joint can be compared with a ball and socket joint; hence, the force needed to overcome the gravity can be represented as a torque about this joint. Assuming an equal mass distribution of the human arm, the point of application of the gravity force, i.e., $\vec{F}_g$, is in the middle of the arm at a length, i.e., l, from the shoulder joint, as shown in Fig. 2(b). The intended target group, which consists of people suffering from a neuromuscular disorder, has an average arm mass of about 3 kg [6] and an arm length of about 0.8 m as given in Table I. In general, the motions for the human arm are defined for the horizontal flexion movement, i.e., ϕ_h, as shown in Fig. 2(a) and, for the flexion/abduction movement, i.e., θ_h, as shown in Fig. 2(b) [14]. Note that, the rotation direction of θ_h is in the reversed direction of the stationary coordinate system θ_s. The specification of the range of motion is given in Table I.

The torque needed to overcome the gravity, which occurs during the flexion/abduction movement, can be determined using

$$T_{xs} = -F_g \sin(\theta_h)\sin(\phi_h)l \tag{1}$$
$$T_{ys} = F_g \sin(\theta_h)\cos(\phi_h)l \tag{2}$$

where T_{xs} is the torque about the x_s-axis, T_{ys} is the torque about the y_s-axis and are defined in a right-handed Cartesian coordinate system. The gravity force does not has any influence on the torque about the z-axis T_{zs}.

Expressing the torque in the spherical coordinate system provides a more general expression that corresponds to the horizontal movement, as shown in Fig. 2(a), and vertical movement, as shown in Fig. 2(b). The torque in the spherical coordinate system can be calculated using

$$\vec{T} = \vec{r} \times \vec{F} \tag{3}$$

where

$$\vec{r} = \rho\vec{e}_\rho + 0\vec{e}_\theta + 0\vec{e}_\phi \tag{4}$$
$$\vec{F} = F_\rho\vec{e}_\rho + F_\theta\vec{e}_\theta + F_\phi\vec{e}_\phi \tag{5}$$

where $\vec{e}$ is the unity vector in the direction described by its subscript, and ρ is the radius and results in

$$T_{\rho s} = 0 \tag{6}$$
$$T_{\theta s} = -\rho F_\phi \tag{7}$$
$$T_{\phi s} = \rho F_\theta. \tag{8}$$

According to the cross product, the direction of rotation for T_{θ_s} is in the reverse ϕ_s-direction, which corresponds with the horizontal movement, as shown in Fig. 2(a), and the direction of rotation for T_{ϕ_s} is in the θ_s-direction, which corresponds with the vertical movement, as shown in Fig. 2(b). Converting the Cartesian coordinate system to the spherical coordinate system results in

$$T_{\theta s} = \cos(\theta_s)\cos(\phi_s)T_{xs} + \cos(\theta_s)\sin(\phi_s)T_{ys} - \sin(\theta_s)T_{zs} \tag{9}$$
$$T_{\phi s} = -\sin(\phi_s)T_{xs} + \cos(\phi_s)T_{ys}. \tag{10}$$

The torque, i.e., T_{xs} (1), depends on the angle θ_h, where at $\theta_h = 180^\circ$ and $\theta_h = 0^\circ$, no shoulder joint torque is required to keep the human arm in position. However, at an angle of $\theta_h = 90^\circ$, a maximum shoulder joint torque is needed to overcome the gravity.

All human bodies differ from each other; therefore, to optimize and design a realistic and suitable gravity compensator, average numbers of the target group are taken into account. The intended target group, which consists of people suffering from a neuromuscular disorder, has an average arm mass of 3 kg [15] and an arm length of 0.8 m. Therefore, the application point of the gravity force, i.e., F_g, is situated on a distance of the shoulder at $l = 0.4$ m. Hence, the gravity compensator must counterbalance for a maximum torque of $T_{\max} = 12\ \mathrm{N}\cdot\mathrm{m}$.

For this application, a range of motion of several basic ADLs is considered, such as stretching forward, drinking, eating,

and using the computer. All these activities require flexion/abduction movement [14] ranging from typically $\theta_h = 0^\circ$ to $\theta_h = 90^\circ$ [16] and a horizontal flexion movement [14] ranging from $\phi_h = 40^\circ$ to $\phi_h = 130^\circ$.

For the design of the spherical gravity compensator, it is assumed that the human arm has an equal mass distribution. In reality, there is a difference in mass between the upper arm and the combination of the forearm, wrist, and hand of about 0.6% of the total human mass [17]. Furthermore, rotation of the elbow changes the required torque as the mass distribution alters. This change in torque depends on the mechanical construction of the arm support system, the number of support points, and where the arm is supported. When these dependencies are known, one could calculate the worst case scenarios and could choose an averaged solution. Considering two equally distributed masses, one for the upper arm and one for the combination of the forearm, wrist, and hand, the required torque difference between the worst case scenarios, namely, stretched arm and bent arm, is about 4.5 N · m. In this calculation, the compensation movements of the user are not included. Compensation movements occur when a human arm with, for example, deteriorated muscles, needs to compensate for lost arm functionality during certain movement trajectories. These movements can change the expected torque requirement.

The presented design of the spherical gravity compensator considers a worst case scenario, namely, a stretched arm perpendicular to the gravity force. Depending on the mechanical design of the arm support and practical tests, it could be possible that the size of the gravity compensator can be decreased.

III. Topologies

A. Working Principle

The proposed magnetic gravity compensator consists of two semispherical permanent magnets, as shown in Fig. 1, where the inner semisphere can rotate freely in the θ_s- and ϕ_s-direction. From Fig. 2(b), it is shown that at the starting position, i.e., $\theta_h = 0^\circ$, no compensation is required. By an increasing angle θ_h, an increasing positive torque is needed; hence, at the starting position, a metastable position is required. An increasing torque is necessary until $\theta_h = 90^\circ$, where it reaches its maximum. From this position, a decreasing torque is necessary until $\theta_h = 180^\circ$, where no torque is needed; hence, a stable position is required at $\theta_h = 180^\circ$. However, because only a limited range of motion is considered, the stable position will not be reached. Furthermore, the torque characteristic should be sinusoidal between the stable and metastable points.

B. Method

To obtain this sinusoidal torque characteristic, different magnetizations are investigated, as shown in Fig. 3, to find the most suitable topology applicable for arm support systems. The initial geometry parameters for this investigation are shown in Table II and defined in Fig. 4. The torque characteristic of all combinations of parallel and radial magnetization of the two magnets is obtained. To validate the consistency of the torque characteristic, the torque of three different ratios between the inner magnet thickness and the outer magnet thickness is investigated. The ratio between the two magnets is defined as

$$\alpha = \frac{R_{\text{in}}}{R_{\text{out}}}. \tag{11}$$

The torque in the spherical coordinate system can be obtained using the Maxwell stress tensor [18], i.e.,

$$\vec{T} = r \times \frac{1}{\mu} \oint_S \mathbb{T} \cdot \vec{n}\, ds \tag{12}$$

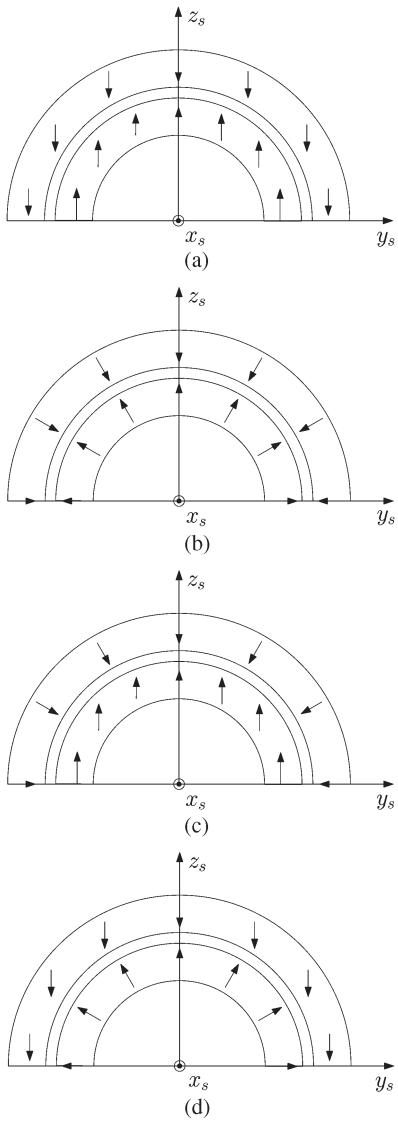

Fig. 3. Magnetization topologies of the outer and the inner semisphere, respectively, (a) parallel–parallel, (b) radial–radial, (c) radial–parallel, and (d) parallel–radial.

TABLE II
Initial Geometry Parameters

Parameter	Value	Unit	Description
R_{rod}	15	mm	Radius of the rod
R_{in}	25.2	mm	Outer radius of the inner magnet
g	1	mm	Airgap length
R_{out}	36	mm	Outer radius of the outer magnet
B_{rem}	1.23	T	Remanent magnetic flux density
μ_r	1.05	-	Relative permeability

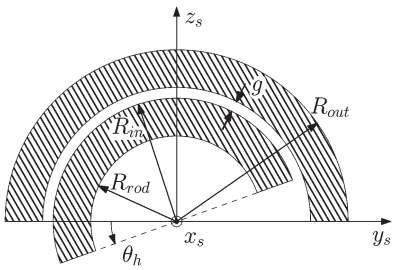

Fig. 4. Definition of the geometry parameters.

where $\vec{r}$ is the displacement vector and

$$\mathbb{T}_{nm} = B_n B_m - \delta_{nm} \frac{1}{2} B_k^2 \tag{13}$$

where

$$\delta_{ij} = \begin{cases} 1, & \text{for } i = j \\ 0, & \text{for } i \neq j. \end{cases} \tag{14}$$

Defining the point of application at the origin, the displacement vector $\vec{r}$ is defined as

$$\vec{r} = \begin{bmatrix} \rho \vec{e}_\rho \\ 0 \vec{e}_\theta \\ 0 \vec{e}_\phi \end{bmatrix} \tag{15}$$

and the Maxwell stress tensor is defined as

$$\mathbb{T} = \begin{bmatrix} B_\rho^2 - \frac{1}{2}|\vec{B}|^2 & B_\rho B_\theta & B_\rho B_\phi \\ B_\theta B_\rho & B_\theta^2 - \frac{1}{2}|\vec{B}|^2 & B_\theta B_\phi \\ B_\phi B_\rho & B_\phi B_\theta & B_\phi^2 - \frac{1}{2}|\vec{B}|^2 \end{bmatrix}. \tag{16}$$

Subsequently, the torque components can be obtained by integrating over the airgap surface

$$T_{\theta s} = -\frac{\rho}{\mu} \int_0^{\pi} \int_0^{2\pi} B_\phi B_\rho \, d\theta \, d\phi \tag{17}$$

$$T_{\phi s} = \frac{\rho}{\mu} \int_0^{\pi} \int_0^{2\pi} B_\theta B_\rho \, d\theta \, d\phi. \tag{18}$$

Considering the magnetization topology as shown in Fig. 3(c), it can be seen from the magnetic flux density in the middle of the spherical airgap, as shown in Fig. 5(a) and (b), that the magnetic flux densities, i.e., B_ρ and B_θ, are independent of ϕ_s at position $\theta_h = 0°$ and $\phi_h = 90°$, respectively. Furthermore, it can be seen in Fig. 5(c) that the obtained B_ϕ is negligible. Therefore, it can be concluded from (17) that there is no torque $T_{\theta s}$, and $T_{\phi s}$ is independent from ϕ_s (18), which holds for all ϕ_h. Hence, torque T_{xs} obtained at $\phi_s = 90°$ is equal to the negative torque $T_{\phi s}$, and the expected 3-D performance can be derived from 2-D FEA.

The spherical structure is represented in a 2-D cylindrical FEA model with depth d. This depth can be obtained by using the ratio between the effective airgap areas. The effective airgap area of the 2-D rotary structure is

$$A_{\text{cylinder}} = \frac{2\pi \left(R_{\text{in}} + \frac{g}{2}\right) d}{2} \tag{19}$$

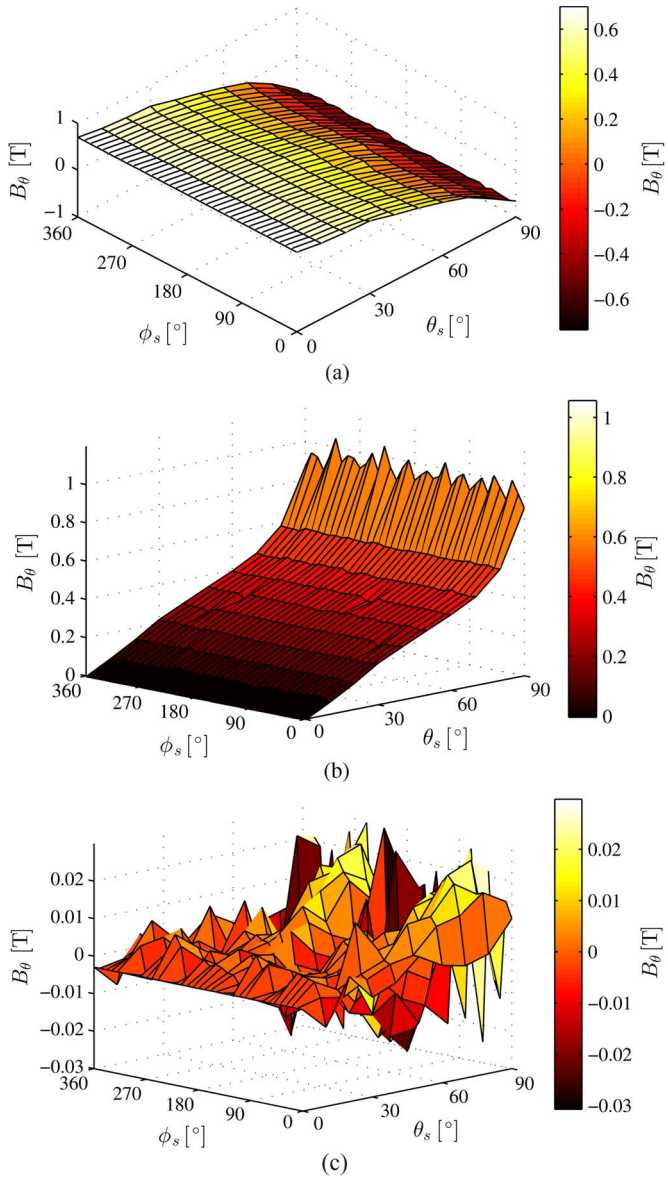

Fig. 5. Magnetic flux density components in the middle of the airgap at position of $\theta_h = 0°$ and $\phi_h = 0°$, (a) B_ρ, (b) B_θ, and (c) B_ϕ.

where R_{in} is the radius of the inner magnet, and the effective area of the semisphere is

$$A_{\text{sphere}} = \frac{4\pi \left(R_{\text{in}} + \frac{g}{2}\right)^2}{2}. \tag{20}$$

The ratio between both areas is

$$\frac{A_{\text{sphere}}}{A_{\text{cylinder}}} = \frac{8\pi \left(R_{\text{in}} + \frac{g}{2}\right)^2}{4\pi \left(R_{\text{in}} + \frac{g}{2}\right) d} \tag{21}$$

$$= \frac{2\left(R_{\text{in}} + \frac{g}{2}\right)}{d}. \tag{22}$$

Assuming a ratio of

$$\frac{A_{\text{sphere}}}{A_{\text{cylinder}}} = 1 \tag{23}$$

the depth of the 2-D cylindrical FEA model can be obtained by

$$d = 2\left(R_{\text{in}} + \frac{g}{2}\right). \tag{24}$$

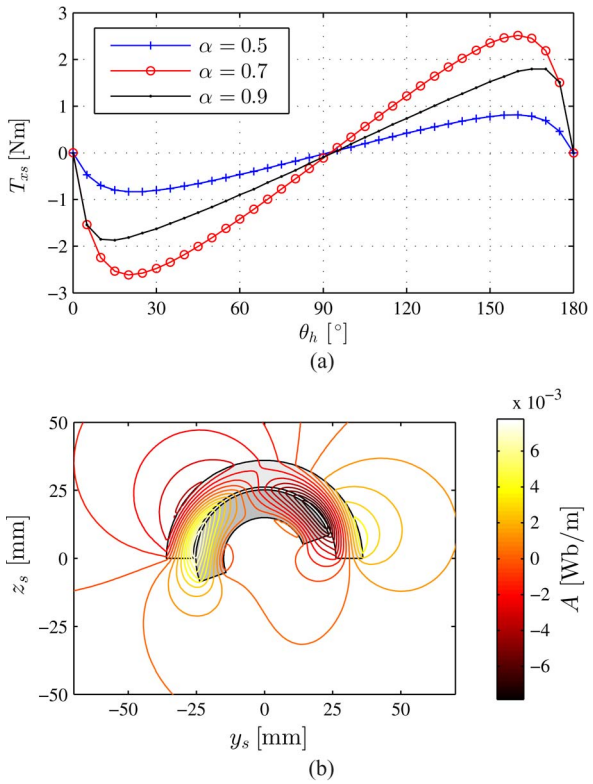

Fig. 6. Parallel–parallel magnetization topology with (a) the torque distribution and (b) the flux line distribution shown for $\theta_h = 20°$.

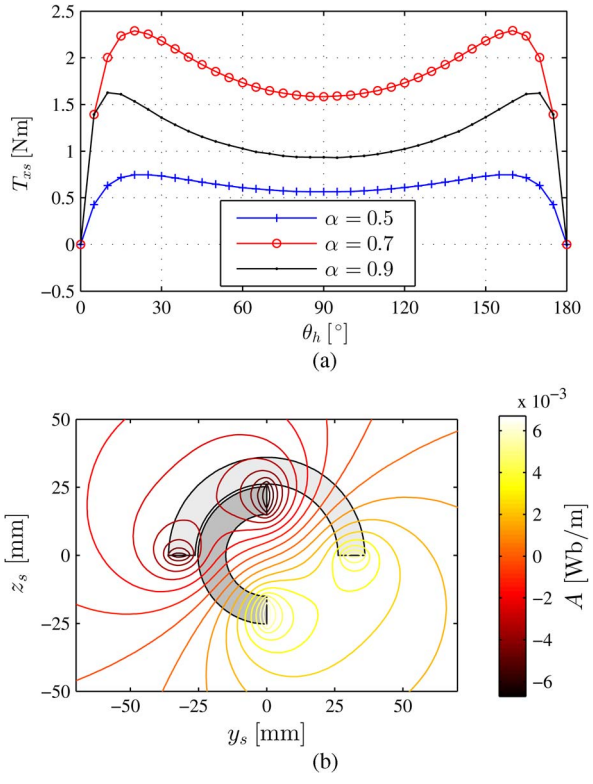

Fig. 7. Radial–radial magnetization topology with (a) the torque distribution and (b) the flux line distribution shown for $\theta_h = 90°$.

C. Results

Using the parallel magnetization for both the inner and outer magnet results in a torque characteristic, as shown in Fig. 6(a). It can be seen that this magnetization has a linear torque characteristic within a range from $\theta_h = 30°$ to $\theta_h = 150°$. Furthermore, it can be seen that, for the three ratios, i.e., $\alpha = 0.5$, $\alpha = 0.7$, and $\alpha = 0.9$, only the amplitude changes and not the characteristic. The highest amount of torque is obtained with $\alpha = 0.7$. Because there is no torque production at position $\theta_h = 90°$, the flux lines are shown at position $\theta_h = 20°$ in Fig. 6(b). Although this linear torque characteristic is not suitable for a mobile arm support, it can be useful for other applications.

Using a radial magnetization for both magnets results in a torque characteristic, as shown in Fig. 7(a). This torque has a nonlinear characteristic over the range of $\theta_h = 0°$ to $\theta_h = 90°$, which is also not suitable for the mobile arm support system application. In addition, for this magnetization topology, it holds that $\alpha = 0.7$ provides the highest amplitude, and there is no change in the characteristic of torque. The flux lines at a position of $\theta_h = 90°$ are shown in Fig. 7(a).

Combining these two magnetization topologies, a radial magnetization for the outer magnet and a parallel magnetization for the inner magnet result in a torque characteristic, as shown in Fig. 8(a). This figure illustrates the desired sinusoidal torque characteristic as required in (1), independently from ratio α. The flux lines at a position of $\theta_h = 90°$ are shown in Fig. 8(a).

Inverting the previous topology, a parallel magnetization for the outer magnet and a radial magnetization for the inner magnet results in a torque characteristic, as shown in Fig. 9(a). In addition, this topology gives a sinusoidal characteristic.

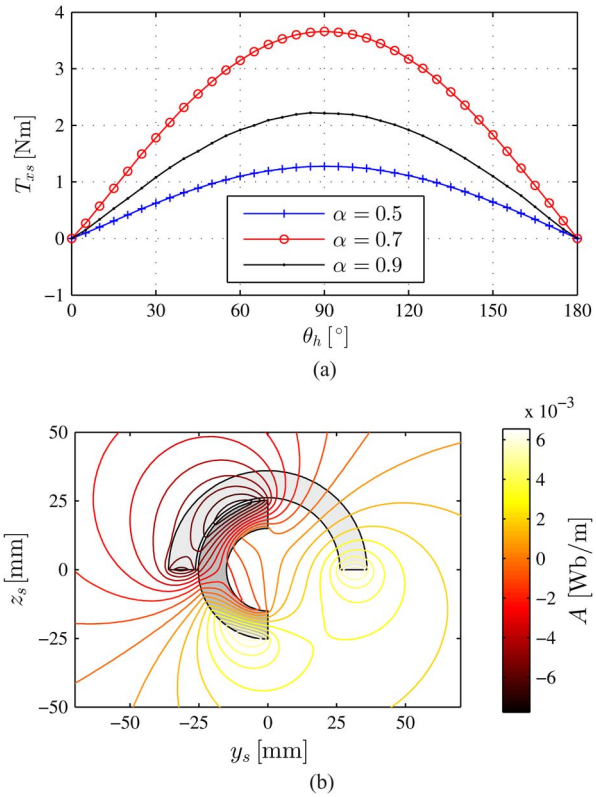

Fig. 8. Radial–parallel magnetization topology with (a) the torque distribution and (b) the flux line distribution shown for $\theta_h = 90°$.

However, the torque level is very small, and therefore, the numerical noise of the FEA becomes more visible. From the flux lines, as shown in Fig. 9(b), it can be seen that the magnetic

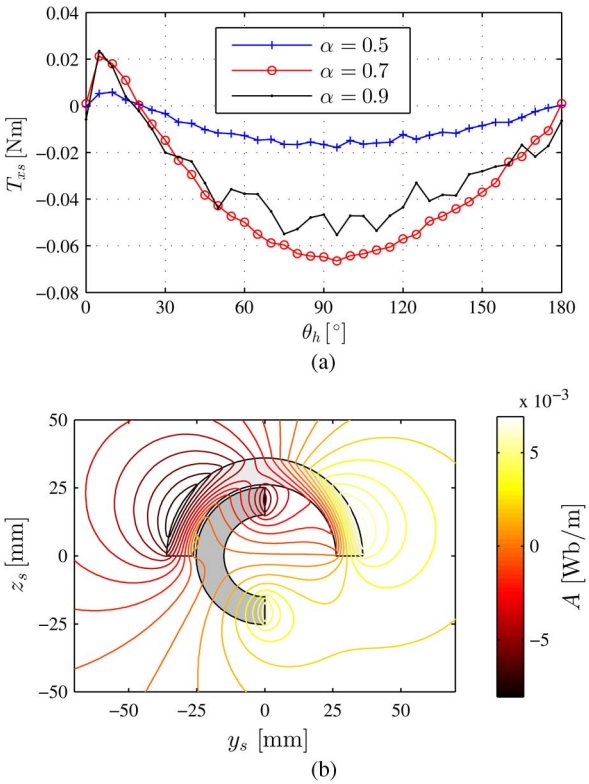

Fig. 9. Parallel–radial magnetization topology with (a) the torque distribution and (b) the flux line distribution shown for $\theta_h = 90°$.

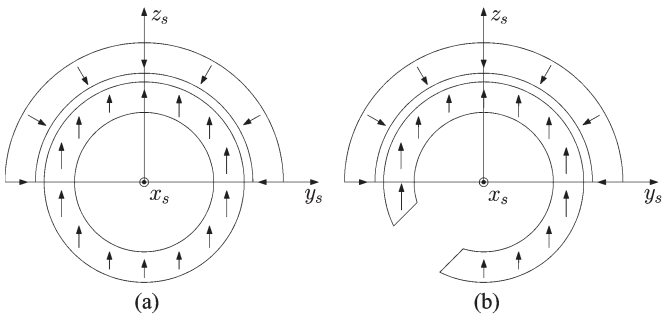

Fig. 10. Different geometries for the radial–parallel magnetization topology. (a) Sphere geometry for the inner magnet. (b) Sphere geometry with cutout to mount the rod for the inner magnet.

field of the outer magnet has short circuited itself. Therefore, almost no flux from the outer magnet enters the inner magnet and almost no torque is generated.

The topology using the radial magnetization combined with the parallel magnetization for the outer and inner magnet, respectively, is further analyzed because it provides the sinusoidal characteristic with the highest amplitude.

IV. Geometry Optimization

This section considers the topology chosen as the most suitable solution in Section III. This topology is optimized for the smallest size to reduce the costs of the magnetic gravity compensator.

To optimize the geometry for the required torque level, different inner magnet shapes are investigated. A spherical magnet, as shown in Fig. 10(a), can be used as the inner magnet. Because a rod is needed to exert the created torque, a full sphere is

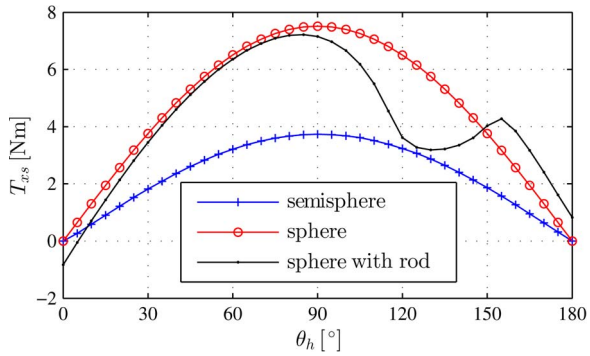

Fig. 11. Torque, i.e., T_{xs}, for the different inner magnet geometries: semisphere, sphere, and sphere with rod.

TABLE III
Error Between the Different Geometries, Semisphere, Sphere, and Sphere With Rod Torque Characteristic and the Mathematical Sine Function

Geometry	ϵ_1 (error)
Semisphere	0.75%
Sphere	0.006 %
Sphere with rod	4.3%

difficult to realize in practice. Therefore, a solution is shown in Fig. 10(b), where a segment is left out for the rod. Both torque characteristics are shown in Fig. 11 and compared with the semispherical inner magnet. It can be seen that the full sphere has almost twice the torque of a semispherical magnet and the sphere with the rod cutout no longer has sinusoidal characteristic. The error between the normalized torque and the mathematical sine function is calculated using

$$\epsilon_1 = \text{rms}\left(\frac{T(\theta_h)}{\max(T)} - \sin(\theta_h)\right) \tag{25}$$

over the specified range of $\theta_h = 0°$ and $\theta_h = 90°$ for all three of the geometry topologies. The resulting errors are given in Table III. Ideally, the spherical-shaped permanent magnet is the best topology; however, it has an unpractical geometry. The spherical-shaped magnet with rod topology compensates the gravity over a range of $\theta_h = 5°$ to $\theta_h = 85°$; therefore, it does not meet the specifications. The semispherical-shaped magnet complies with all the specifications; therefore, this topology is further optimized.

Optimization is performed on the geometry parameters, i.e., R_{in} and R_{out}, to find the smallest size capable of delivering the required torque. For this optimization, the airgap, i.e., g, and the rod radius, i.e., R_{rod}, are kept constant as their values, mentioned in Table II, are already set to a minimum. The torque generation for the different magnet sizes is obtained at position $\theta_h = 90°$ and shown in Fig. 12, where the black line represents the specified $T_{\max} = 12$ N · m. It is found that the most optimal parameters are $R_{\text{in}} = 36$ mm and $R_{\text{out}} = 49$ mm.

V. Three-Dimensional Verification

The analysis is performed using 2-D FEA to predict the performance for different ratios between the inner magnet and outer magnet size. For verification of the most optimal design, the 3-D model, as shown in Fig. 1, is applied. In Fig. 13, the results from the optimized 2-D FEA topology are compared with

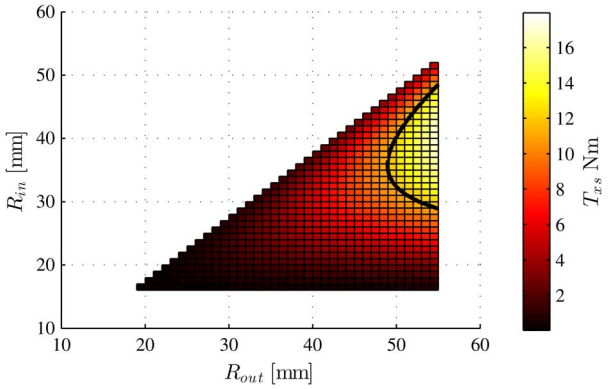

Fig. 12. Torque, i.e., T_{xs}, as a function of the radii $R_{\rm in}$ and $R_{\rm out}$ obtained from the position of $\theta_h = 90°$, where the black line represents the specifications of $T_{\rm max}$.

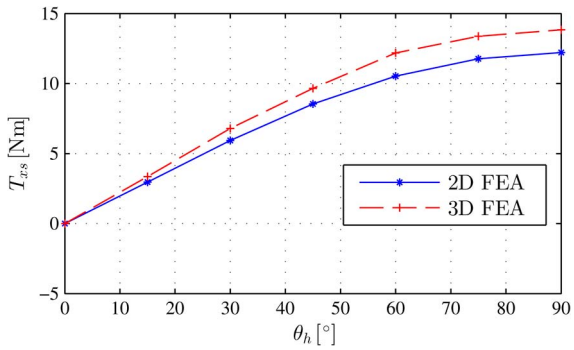

Fig. 13. FEA results of the 2-D and 3-D simulation for the optimal radii, i.e., $R_{\rm in} = 36$ mm and $R_{\rm out} = 49$ mm.

the obtained 3-D FEA. A discrepancy of 8.7% occurs between these results and is considered acceptable. This discrepancy is calculated using

$$\epsilon_2 = \text{rms}\left(\frac{T_{3D} - T_{2D}}{\max(T_{3D})}\right). \tag{26}$$

The 3-D torque results are higher with respect to the 2-D results, which can be explained by the end effects. Considering the ratio between the torque generated and the surface area in the middle of the airgap, i.e., the shear stress, the torque can be obtained by

$$T = r_g^3 4\pi\sigma \tag{27}$$

where σ is the shear stress, and r_g the radius of the airgap. It can be seen that the torque changes with the power of three in function of the radius. Therefore, a small change in size will result in a relatively large change in torque. Hence, redesigning the 3-D model from the found 13 N · m to the specified 12 N · m decreases the radius at about 4%.

The optimum solution is obtained in the 2-D FEA, for the smallest size of $R_{\rm out} = 49$ mm; however, it has been verified that this is also an optimal solution in the 3-D domain. To verify this, without performing the complete optimization again in 3-D, a surface map of the torque in the specified range of motion and for $R_{\rm in} = 34$ mm to 37 mm is performed. From this analysis, shown in Table IV, it can be concluded that for each point $R_{\rm in} = 36$ mm is equal or has a higher torque than the other radii.

TABLE IV
TORQUE RESULTS: $T_{\phi s}$ AT DIFFERENT θ_h POSITIONS

θ_h	R_{in}=34 mm	R_{in}=35 mm	R_{in}=36 mm	R_{in}=37 mm
0°	0 Nm	0 Nm	0 Nm	0 Nm
45°	9.6 Nm	9.7 Nm	9.7 Nm	9.5 Nm
90°	13.8 Nm	13.9 Nm	13.9 Nm	13.7 Nm

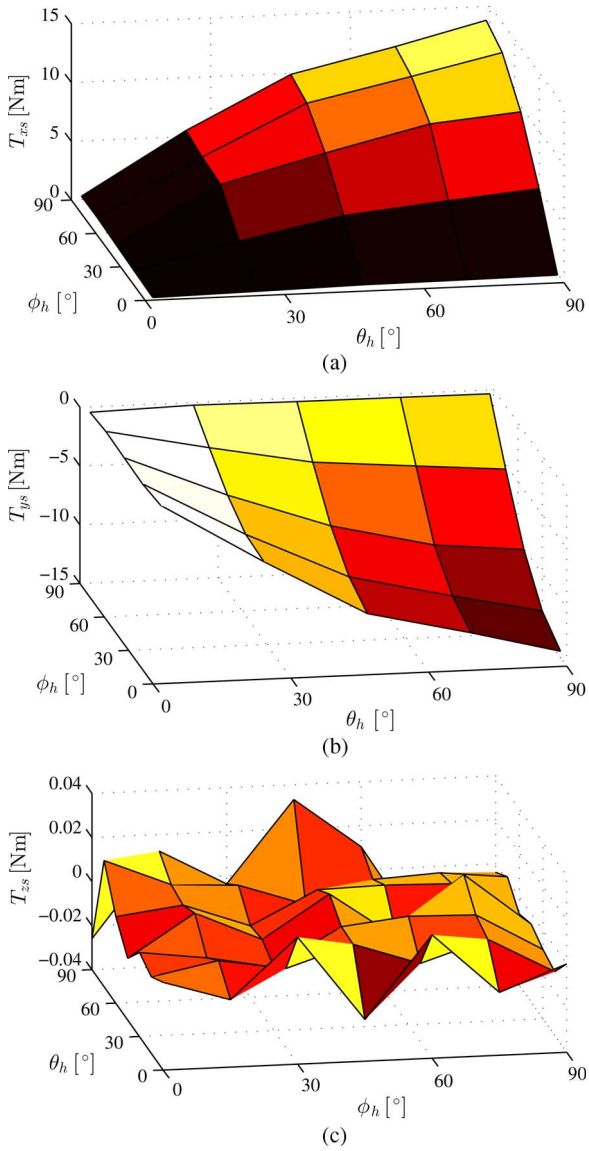

Fig. 14. Three-dimensional FEA results for the optimal radii, i.e., $R_{\rm in} = 36$ mm and $R_{\rm out} = 49$ mm, as a function of θ_h and ϕ_h for (a) T_{xs}, (b) T_{ys}, and (c) T_{zs}.

From torque results of T_{xs} and T_{ys}, as shown in Fig. 14(a) and (b), it can be seen that the characteristic is in agreement with (1) and (8), respectively. Torque T_{zs} is shown in Fig. 14(c) and consists of numerical noise. The spherical torque $T_{\phi s}$ is shown in Fig. 15; it is shown that this torque is independent of ϕ_h and has the expected sinusoidal characteristic.

Determining the error between the obtained 3-D results and a mathematical sine function, the rms error (25) is used. The error obtained for $T_{\phi s}$ is $\epsilon_1 = 0.7\%$. From these results, it is concluded that the proposed magnetic gravity compensator is capable of delivering the desired torque density.

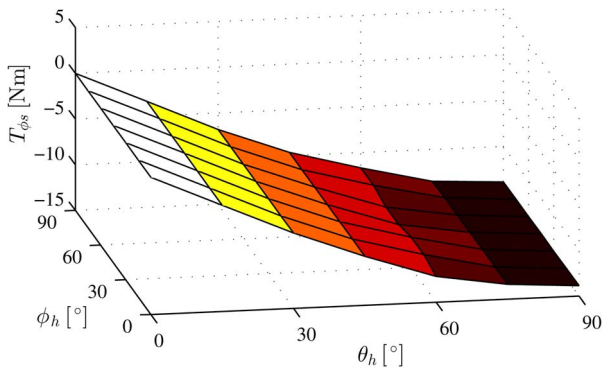

Fig. 15. Three-dimensional FEA results for the optimal radii, $R_{\text{in}} = 36$ mm and $R_{\text{out}} = 49$ mm: $T_{\phi s}$ as a function of θ_h and ϕ_h.

TABLE V
FORCES EXERTING ON THE INNER SPHERICAL PERMANENT MAGNET

θ_h [deg]	F_x [N]	F_y [N]	F_z [N]
0	0.075	-0.081	633
15	-183.25	0.082	448.71
30	-192.64	0.014	207
45	-160.8	0	59
60	-111	0.25	119
75	-52.6	-0.2	-107
90	9	0.05	-129.7

VI. ADDITIONAL DESIGN ASPECTS

Providing stable movement, special bearing must be designed that is capable of keeping the two spherical permanent magnets concentric. Because two opposite polarized magnets are used, it is expected that repelling forces will be present. Therefore, the forces exerted on the spherical permanent magnets are investigated. The forces that are exerted on the inner spherical permanent magnet are shown in Table V for different positions. Note that the force in the z-direction is attractive until the inner spherical permanent magnet rotates more than 60°.

The design considers two permanent magnets that are magnetized in opposite directions. Therefore, there is a possibility that the magnets will be demagnetized globally or locally. The highest risk of demagnetization in the outer magnet with a radial magnetization is shown in Fig. 16(a). It can be seen that the probability of demagnetization is the highest in the center of the magnet. Due to the radial magnetization, the flux in the outer spherical magnet goes to the edges of the sphere. This means that the flux density is the lowest in the center at the sphere and, therefore, the most vulnerable for demagnetization. The inner spherical permanent magnet with parallel magnetization has a risk of demagnetization, as shown in Fig. 16(b). It can be seen that the risk of demagnetization is the highest on a small part in the center and on the outer edges. The flux density of the outer spherical permanent magnet is the highest on the edges, which causes the demagnetization at the edges of the inner spherical permanent magnet. The demagnetization in the center of the inner spherical permanent magnet is caused by its own flux, which tends to return through the center of the spherical gravity compensator. However, compared with the outer permanent magnet, the demagnetization risk is lower. As can be concluded from these figures, the danger of local demagnetization is high, particularly for the outer permanent magnet. Therefore, minimal intrinsic coercivity must be considered of 1100 kA/m,

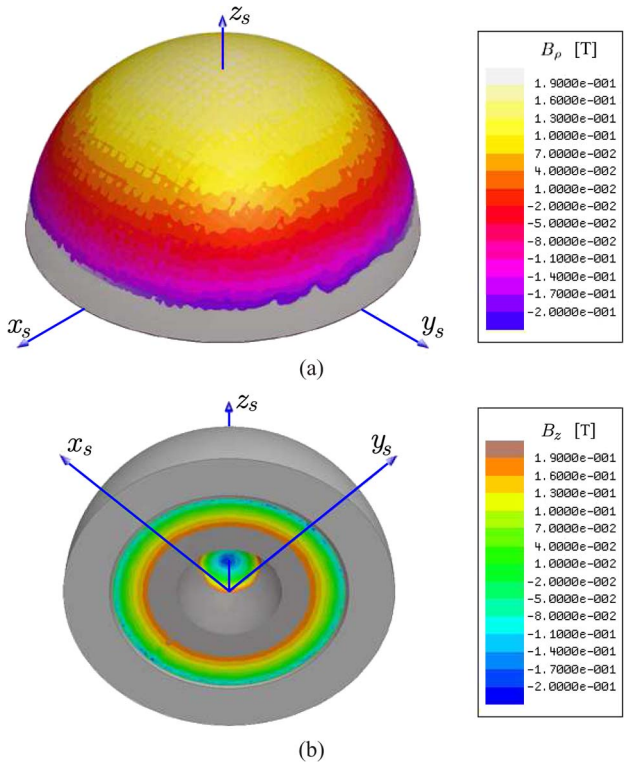

Fig. 16. Magnetic flux density in the areas where the risk of local demagnetization is the highest of (a) outer magnet and (b) inner magnet.

which corresponds with a magnetic flux density of −0.2 T should be accounted for when the permanent magnet material is selected for the prototype.

The proposed spherical gravity compensator is composed from permanent magnets. For a medical application, the magnetic field that is created and surrounds the compensator cannot be neglected. However, because the magnets are oppositely polarized, the magnetic field tends to stay inside the structures and airgap. The magnetic flux density drops to 0.1 T at 10-mm distance and to 0.5 mT at 50-mm distance from the spherical gravity compensator. To decrease this magnetic field further, a magnetic shield can be applied.

VII. CONCLUSION

A novel magnetic gravity compensator has been proposed for the application of mobile arm support systems. It has been shown that the proposed concept is capable of providing the specified torque characteristic for this application. It has been found that the most suitable magnetization to achieve this characteristic is a radial magnetization for the outer magnet and a parallel magnetization for the inner magnet. From the 2-D optimization, it has been shown that the smallest size to achieve the specified torque of $T_{\max} = 12$ N · m was obtained. However, reducing the range of motion such that the spherical magnet with rod topology would meet the specification, a smaller sized spherical magnetic gravity compensator could be realized. The obtained optimized 2-D results have been verified using 3-D FEA. From the found results it has been shown that the gravity compensator can be realized within a size of a sphere with a radius of $R_{\text{out}} = 49$ mm. This is an acceptable size for mobile arm support systems; therefore, the magnetic gravity compensator is an advanced and efficient solution.

REFERENCES

[1] J. L. Herder, N. Vrijlandt, M. Antonides, T. Cloosterman, and P. L. Mastenbroek, "Principle and design of a mobile arm support for people with muscular weakness," *J. Rehabil. Res. Develop.*, vol. 43, no. 5, pp. 591–604, 2006.

[2] G. Kramer, G. R. B. Romer, and H. J. A. Stuyt, "Design of a dynamic arm support (DAS) for gravity compensation," in *Proc. ICORR*, 2007, pp. 1042–1048.

[3] T. Nef and R. Riener, "Shoulder actuation mechanisms for arm rehabilitation exoskeletons," in *Proc. 2nd IEEE RAS EMBS Int. Conf. BioRob.*, 2008, pp. 862–868.

[4] C. R. Carignan, M. P. Naylor, and S. N. Roderick, "Controlling shoulder impedance in a rehabilitation arm exoskeleton," in *Proc. ICRA*, May 2008, pp. 2453–2458.

[5] H. Li, C. Xia, and T. Shi, "Spherical harmonic analysis of a novel Halbach array PM spherical motor," in *Proc. IEEE Int. Conf. ROBIO*, 2007, pp. 2085–2089.

[6] H. Son and K.-M. Lee, "Open-loop controller design and dynamic characteristics of a spherical wheel motor," *IEEE Trans. Ind. Electron.*, vol. 57, no. 10, pp. 3475–3482, Oct. 2010.

[7] W. Wang, J. Wang, G. W. Jewell, and D. Howe, "Design and control of a novel spherical permanent magnet actuator with three degrees of freedom," *IEEE/ASME Trans. Mechatronics*, vol. 8, no. 4, pp. 457–468, 2003.

[8] T. Yano, Y. Kubota, T. Shikayama, and T. Suzuki, "Basic characteristics of a multi-pole spherical synchronous motor," in *Proc. Int. Symp. MHS*, 2007, pp. 383–388.

[9] L. Yan *et al.*, "Design and analysis of a permanent magnet spherical actuator," in *Proc. IEEE/RSJ Conf. IROS*, 2005, pp. 691–696.

[10] K. Kahlen, I. Voss, C. Priebe, and R. W. De Doncker, "Torque control of a spherical machine with variable pole pitch," *IEEE Trans. Power Electron.*, vol. 19, no. 6, pp. 1628–1634, Nov. 2004.

[11] L. Encica, J. J. H. Paulides, and E. A. Lomonova, "Space-mapping optimization in electromechanics: An overview of algorithms and applications," *COMPEL, Int. J. Comput. Math. Elect. Electron. Eng.*, vol. 28, no. 5, pp. 1216–1226, 2009.

[12] J. L. G. Janssen, J. J. H. Paulides, and E. A. Lomonova, "Study of magnetic gravity compensator topologies using an abstraction in the analytical interaction equations," *Progr. Electromagn. Res., PIER*, vol. 128, no. 1, pp. 75–90, 2012.

[13] J. L. G. Janssen, B. L. J. Gysen, J. J. H. Paulides, and E. A. Lomonova, "Advanced electromagneic modeling applied to anti-vibration systems for high precision and automotive applications," *Int. Compumag Soc. Newslett.*, vol. 19, no. 1, pp. 3–16, 2012.

[14] I. A. Kapandji, *The Physiology of the Joints (Upper Extremities)*, 5th ed. London, U.K.: Churchill Livingstone, 1982.

[15] V. L. Nickel, J. R. Kachak, and J. R. Allen, "Electrically powered orthotic systems," *J. Bone J. Surg.*, vol. 51-A, no. 2, pp. 343–351, 1969.

[16] G. R. Johnson, D. A. Carus, G. Parrini, S. Scattereggia Marchese, and R. Valeggi, "The design of a five-degree-of-freedom powered orthosis for the upper limb," *Proc. Inst. Mech. Eng., J. Eng. Med.*, vol. 215, no. 3, pp. 275–284, 2001.

[17] D. A. Winter, *Biomechanics and Motor Control of Human Movement*. Hoboken, NJ, USA: Wiley, 2009.

[18] H. Woodson and J. Melcher, *Electromechanical Dynamics, Part II: Field, Forces, and Motion*. New York, NY, USA: Wiley, 1968.

B. van Ninhuijs (S'12) was born in The Netherlands. He received the M.Sc. degree in electrical engineering from Eindhoven University of Technology, Eindhoven, The Netherlands, in 2011, where he is currently working toward the Ph.D. degree in the Group of Electromechanics and Power Electronics.

J. W. Jansen (S'03–M'07) received the M.Sc. degree (*cum laude*) in electrical engineering and the Ph.D. degree in magnetically levitated planar actuator technology from Eindhoven University of Technology, Eindhoven, The Netherlands, in 2003 and 2007, respectively.

He then joined the Group of Electromechanics and Power Electronics, Eindhoven University of Technology, where he is currently an Assistant Professor. His research interests include magnetic levitation and the analysis and design of linear and planar actuators.

B. L. J. Gysen (S'07–M'07) was born in Bilzen, Belgium, on January 3, 1984. He received the M.Sc. and Ph.D. degrees (*cum laude*) in electrical engineering from Eindhoven University of Technology, Eindhoven, The Netherlands, in 2007 and 2011, respectively.

In 2011, he started his industrial career with Prodrive Technologies, Eindhoven, and continued his scientific career as a part-time Assistant Professor with the Group of Electromechanics and Power Electronics, Eindhoven University of Technology. His research considers analytical electromagnetic modeling and design techniques for linear and rotating actuators for applications in robotics, anti-vibration, and energy harvesting.

E. A. Lomonova (M'04–SM'07) was born in Moscow, Russia. She received the M.Sc. (*cum laude*) and Ph.D. (*cum laude*) degrees from Moscow State Aviation Institute, Moscow, Russia, in 1982 and 1993, respectively, both in electromechanical engineering.

She is currently a Full Professor and Chair of the Group of Electromechanics and Power Electronics, Eindhoven University of Technology, Eindhoven, The Netherlands. She has worked on electromechanical actuators design, optimization, and development of advanced mechatronics systems.